ACS Energy LETTERS

pubs.acs.org/journal/aelccp

Letter

The Impact of C_{60}-Self-Assembled Monolayer Electron-Transport Layers in Negative–Intrinsic–Positive Perovskite Solar Cells

Suer Zhou, Luca Gregori, Seongrok Seo, Raghunath R. Dasari, Jae Eun Lee, Edoardo Mosconi, Heon Jin, Francesca Nunzi, Fengning Yang, Manuel Kober-Czerny, Alexandra J. Ramadan, Akash Dasgupta, Leonardo Pacifici, Igal Levine, Joel Smith, Stephen Barlow, Laura M. Herz, Filippo De Angelis, Seth R. Marder, and Henry J. Snaith*

Cite This: *ACS Energy Lett.* 2026, 11, 6177–6186

Read Online

ACCESS | Metrics & More | Article Recommendations | Supporting Information

ABSTRACT: We investigate the impact of employing fullerene self-assembled monolayers (SAMs) in conjunction with SnO_2 electron-transport layers (ETLs) in negative–intrinsic–positive (n–i–p) perovskite solar cells. We compare the efficacy of the fullerene-SAM surface-binding group—carboxylic or phosphonic acid—on the passivation, charge transport, and energetics of the modified-SnO_2 surface. Planar n–i–p perovskite solar cells with these SAM-modified SnO_2 exhibit significantly reduced hysteresis, and the steady-state maximum power point tracked efficiencies (η_{MPP}) of the devices improved from an average of 18.6–20.0% comparing devices with neat SnO_2 to the C_{60}-PA SAM inclusion, respectively. While C_{60}-PA SAM improved the initial solar cell efficiency, this benefit was not maintained during light exposure at elevated temperatures as the fullerene SAM weakened adhesion at the perovskite/metal oxide interface in the aged devices. These results highlight the importance of improving the mechanical robustness of perovskite/charge-transport layer interfaces under operational aging conditions.

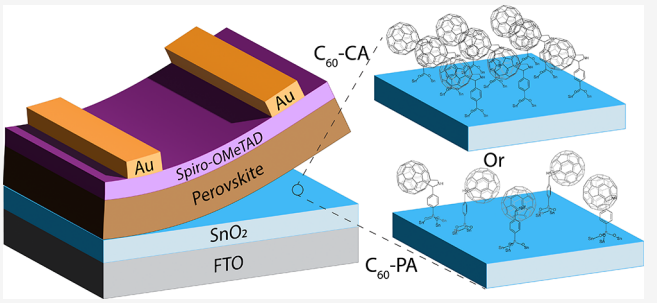

Single-junction planar metal-halide perovskite solar cells (PSCs) have achieved power conversion efficiencies (PCEs) of 28%,[1] on the verge of surpassing those of crystalline silicon solar cells. However, improving operational stability remains a major challenge for PSCs to be a highly competitive commercial technology. In typical planar negative–intrinsic–positive (n–i–p) PSCs, SnO_2 can introduce interfacial nonradiative recombination losses due to trap states associated with undercoordinated Sn ions and/or oxygen vacancies.[2−5] Surface hydroxyl groups at the metal oxide surface can also result in increased hysteresis and degradation in devices.[6] To overcome these issues, fullerene derivatives are commonly applied to the SnO_2/perovskite interface due to their favorable n-type transporting properties and potential for defect passivation.[7,8] For instance, there have been many reports of using C_{60} and [6,6]-phenyl-C61-butyric acid methyl ester (PCBM) as interface modifications for SnO_2 in n–i–p devices to improve the open-circuit voltage and reduce hysteresis in the current–voltage curves.[6,9−12] While C_{60} and PCBM on SnO_2 form a physisorbed passivation layer, C_{60} derivatives bearing an "oxide-binding group" can form so-called self-assembled monolayers (SAMs), i.e., chemisorbed layers, chemically bonded to the surface, which can improve electron injection and reduce nonradiative recombination.[13,14]

Over the last few years, SAM-based hole-transport layers (HTLs) have driven efficiency advances in positive–intrinsic–negative (p–i–n) PSCs, in place of the previously employed polymeric hole conductors, contributing to the current world-record PCEs now being achieved with the p–i–n architecture.[15−20] Notably, these SAM-forming HTLs almost ubiquitously employ phosphonic acid ($PO(OH)_2$, PA) binding groups rather than carboxylic acids (COOH, CA). Similarly, for electron-transport layer (ETL)-SAMs, changing the functional group of the C_{60}-SAM to PA may potentially improve binding at the surface and passivate more defect sites on the oxide surface.[21] If we wish to form a C_{60} monolayer on the SnO_2 surface, while both CA and PA can bind to the SnO_2 surface through covalent bonds, PA binds more strongly to the metal-oxide surface.[22] C_{60}-PA was originally investigated as an ETL in polymer solar cells,[23] and has recently been used by You et al. in a blend with a perovskite.[24] Herein, we compare neat-SnO_2 to 4-(1′,5′-dihydro-1′-methyl-2′*H*-[5,6]fullereno-C_{60}-I_h-[1,9-*c*]-pyrrol-2′-yl)benzoic acid

Received: May 13, 2026
Revised: June 20, 2026
Accepted: June 22, 2026
Published: August 24, 2026

(C_{60}-CA)- and 4-(1′,5′-dihydro-1′-methyl-2′*H*-[5,6]fullereno-C_{60}-I_h-[1,9-*c*]-pyrrol-2′-yl)phenylphosphonic acid (C_{60}-PA)-modified SnO_2 layers as ETLs in n–i–p PSCs.

We performed contact-angle measurements on fullerene SAMs deposited on fluorine-doped tin oxide (FTO) substrates to assess the surface-energy modification and indicate the "wettability" of the perovskite solution for subsequent spin-coating (Figure S4). For reference, the contact angle of water on FTO directly after UV-ozone treatment is ∼15°. The water contact angle of C_{60}-CA-modified FTO increased dramatically to 95°. In comparison, the contact angle of C_{60}-PA modified FTO is around 37°. Molecularly, the SAM molecules are identical apart from the binding groups. However, these surface angle results suggest that the packing of the SAMs and/or the precise chemical surface presented to the water droplet are quite different, i.e., more unbound PA may be present at the exposed surface.

To understand these differences, we conducted X-ray photoelectron spectroscopy (XPS) measurements on C_{60}-PA and C_{60}-CA modified SnO_2 compared to pristine SnO_2 (Figures S5, S6, and Table S2). Although the phosphorus content was below detection limits for the C_{60}-PA-modified substrates, they have a much higher carbon content compared to the control sample, coupled with the reduction in Sn 3d signal and O 1s signal, which are consistent with attachment of the carbon-rich fullerene to the substrate (see Figure 1a,b, C_{60}-SAM binding modes). Comparing C_{60}-CA to C_{60}-PA (Table S3), we see that not only is there more reduction in Sn and O signals, but also the C content is higher for the C_{60}-CA-modified substrate. This result, along with the significant increase in the C_{60}-CA surface contact angle, unexpectedly indicates that there is higher SnO_2 surface coverage with C_{60}-CA SAM. We also measured ultraviolet photoelectron spectroscopy (UPS) of these C_{60}-SAMs, and the results are shown in Figure S7 and Table S4. The results show that the PA SAM-modified surface has a slightly deeper work function than the CA SAM-modified surface.

To rationalize our inferred binding and surface coverage differences, we apply density functional theory (DFT) calculations to investigate two surface coverage scenarios, hereafter referred to as "half" and "full", corresponding to 1 and 2 fullerene molecules adsorbed on the SnO_2 surface per unit area, as shown in Figure 1a,b, for C_{60}, C_{60}-PA, and C_{60}-CA. The "full" coverage represents the densest possible packing achievable on the specifically selected surface. As shown in Table S5, our calculations reveal that the C_{60}-PA exhibits the highest adsorption energies among the three fullerenes, for both half and full coverage. The relatively weak adsorption of the C_{60} arises from its interaction being dominated by van der Waals forces. In contrast, C_{60}-PA demonstrates significantly stronger binding due to the presence of multiple hydroxyl (–OH) groups, which facilitate both covalent and hydrogen bonding with surface Sn/O ions. Meanwhile, the C_{60}-CA, possessing only two potential binding atoms, exhibits intermediate adsorption strength.

We computed the molecular electrostatic potentials (MEPs) for both systems and the dipole moment component perpendicular to the surface (μ_z), the only dipole component relevant for shifting energy levels[25] as shown in Figure 1c. Using the convention that the dipole vector points from positive to negative charge, μ_z is larger (more negative) for C_{60}-PA than for C_{60}-CA. As visualized from the MEPs, negative charge is concentrated on the CA/PA group, while the tertiary amine carries the positive potential. Notably, the increase in μ_z not only corroborates the increase in the adsorption energy but also helps rationalize the experimentally observed upshift in ionization potentials from the UPS.

Moreover, by calculating the energy difference between full and half coverage (Table S5), we can quantify the energetic penalty associated with close packing. Our results indicate that C_{60}-CA shows an energy loss of only 0.37 eV per molecule between half and full coverage, comparable to that of C_{60} (0.43 eV), while C_{60}-PA close packing leads to a significantly larger loss of 0.76 eV. Although adsorption at low coverage is more exothermic for C_{60}-PA than for C_{60}-CA, the stabilization gained when increasing coverage is smaller for PA than for CA, indicating a weaker driving force for close packing in the PA case. Consequently, we have revealed why the C_{60}-PA results in reduced surface coverage compared to C_{60}-CA, despite having a stronger binding group.

By examining the perovskite films grown on FTO/SnO_2, FTO/SnO_2/C_{60}-CA, and FTO/SnO_2/C_{60}-PA under the top view SEM (Figure S9), we observe little difference in apparent SEM grain size and morphologies (Figure S10 and Table S8). The GIWAXS from different incident angles (Figure S11) and corresponding integrated 1D patterns (Figure 1d) also show that there is no improved crystallinity or preferred orientation of the perovskite grown on either of the C_{60}-SAMs compared to that grown on bare SnO_2.

To understand if there is an interfacial effect, we examine the ETL/perovskite "half-stack" samples. Time-correlated single photon counting (TCSPC) measurements of the samples revealed shorter apparent carrier lifetimes for C_{60}-PA-modified interfaces as compared to SnO_2 or C_{60}-CA-modified SnO_2 (Figure 1e), suggesting either enhanced extraction or increased interfacial losses (see detailed discussion in Note S1 and fitting in Figure S13). While photoluminescence quantum yield (PLQY) measurements on those half-stacks follow the same trend as the TCSPC results (i.e., shorter lifetimes correspond to lower PLQY), the differences between samples are only minor (Note S2 and Figure S14). Time-resolved surface photovoltage (SPV) measurements (Figure S15) revealed a notable delay in the SPV rise time for the C_{60}-PA-modified interfaces, consistent with transient electron trapping and delayed electron injection (see detailed discussion in Note S3).

To assess the impact of a C_{60}-SAM modifying layer on the device performance, we fabricate n–i–p PSCs on different ETLs: directly on FTO-coated glass, FTO/SnO_2, FTO/C_{60}-SAM, and FTO/SnO_2/C_{60}-SAM, as shown in Figure 2 and Table 1. The device structure is Glass/FTO/ETL/Perovskite/phenethylammonium iodide (PEAI)/Spiro-OMeTAD/Au. The steady-state open-circuit voltage (V_{oc}) of devices on FTO was 0.61 ± 0.09 V, which by itself is surprising that the devices do work without a dedicated ETL. However, this was improved by adding a C_{60}-PA layer on top of the FTO (0.80 ± 0.05 V) and also improved further by adding a SnO_2 electron-extraction layer either on its own (1.04 ± 0.01 V) or in combination with the C_{60}-SAMs. The combination of C_{60}-PA on top of the SnO_2 gives the best average steady-state V_{oc} (ssV_{oc}) of 1.06 ± 0.01 V, which is also surprising, since this gave the lowest PLQY in the half-stack. The average maximum power point tracked efficiency (η_{MPP}) of devices improved from 18.6 ± 0.7% for FTO/SnO_2 to 19.5 ±0.05% (20.0 ± 2.1% from a separately fabricated batch reported in Table S10) for FTO/SnO_2/C_{60}-PA. However, the η_{MPP} of FTO/SnO_2/C_{60}-CA is slightly lower at 17.8 ± 1.4%. The champion FTO/SnO_2 device has an η_{MPP} of 21.1%, while

https://doi.org/10.1021/acsenergylett.6c01485
ACS Energy Lett. 2026, 11, 6177−6186

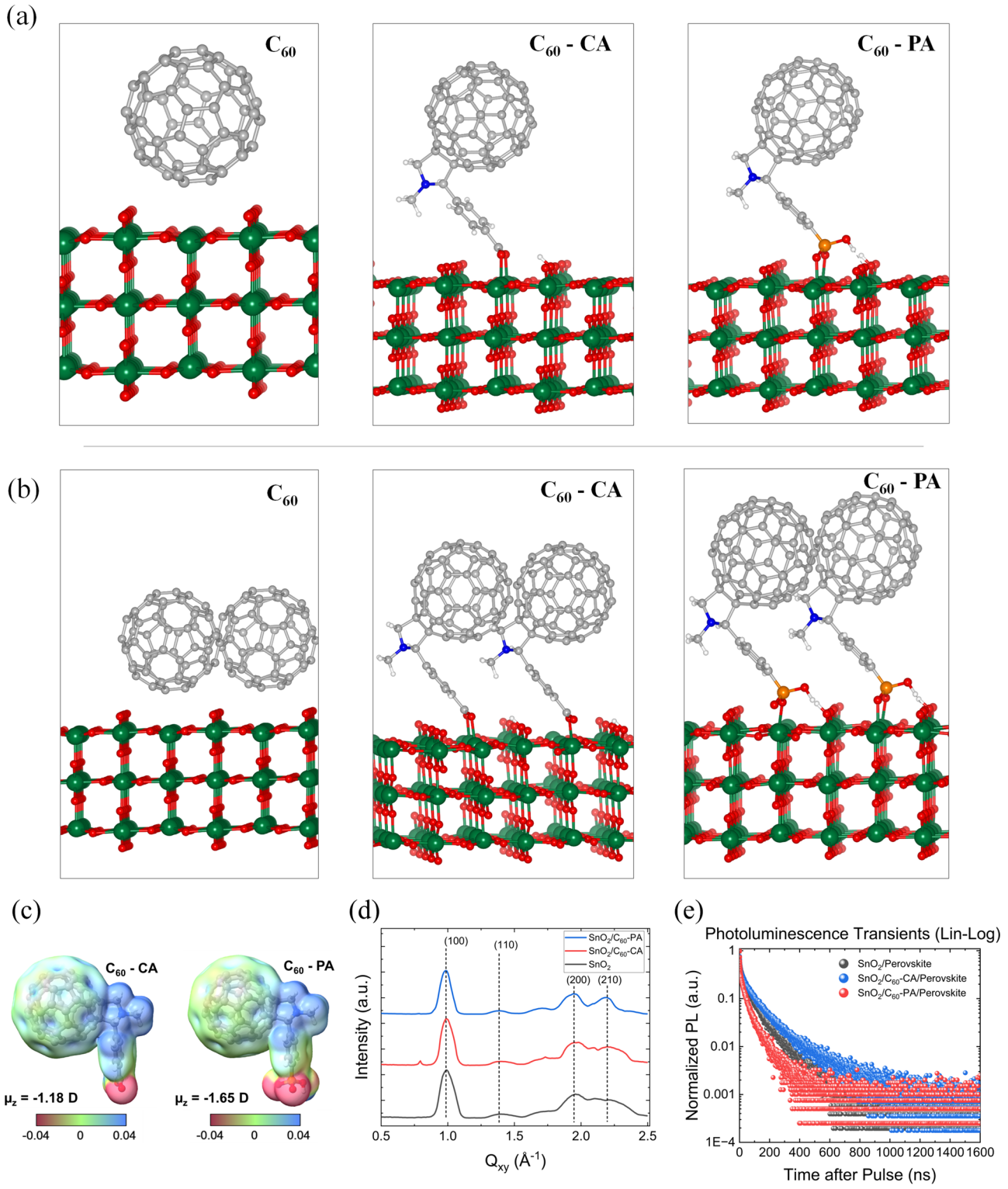

Figure 1. Optimized geometries of the simulated interfaces of (a) "half" and (b) "full" coverage of C_{60}, C_{60}-CA, and C_{60}-PA, respectively. (c) Molecular electrostatic potential maps and calculated dipole moment perpendicular to the surface for the C_{60}-CA and C_{60}-PA, respectively. The isovalue is set to 0.003 au^{-3}. (d) X-ray diffraction (XRD) patterns of $FAPbI_3$ with 35% MACl and 1% $MAPbBr_3$ additive perovskite films on SnO_2, SnO_2/C_{60}-CA, and SnO_2/C_{60}-PA derived from grazing-incidence wide-angle X-ray scattering (GIWAXS). (e) Time-resolved photoluminescence (TRPL) of perovskite processed on three different ETL/perovskite half stacks. The excitation frequency is 300 kHz, 405 nm laser, with a fluence of 196 $nJ{\cdot}cm^{-2}$, measured from the substrate side. See TRPL figures with fittings in the S.I.

https://doi.org/10.1021/acsenergylett.6c01485
ACS Energy Lett. 2026, 11, 6177−6186

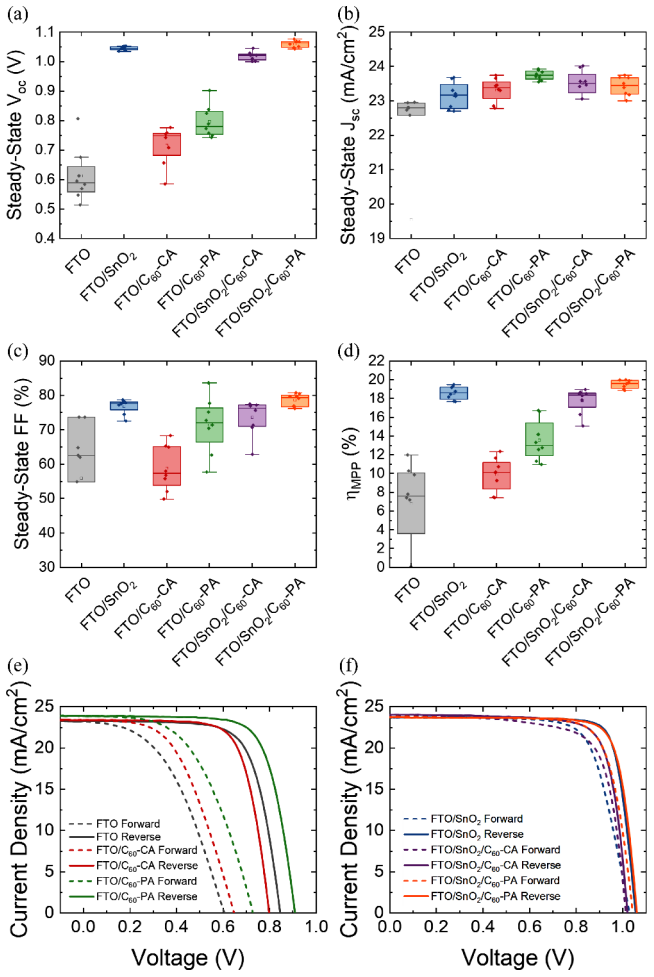

Figure 2. Statistical parameters of devices with structure Glass/FTO/ETL/Perovskite/Spiro-OMeTAD/Au, without any ETL, or SnO_2, C_{60}-CA, C_{60}-PA, SnO_2/C_{60}-CA, and SnO_2/C_{60}-PA as ETLs. (a) Box plot of steady-state open-circuit voltage. (b) Box plot of steady-state short-circuit current density. (c) Box plot of steady-state fill factor. (d) Box plot of maximum power point tracked efficiency. The top and bottom edges of the boxes are the 1st and 3rd quartile, the midline is the median, the top and bottom bars are the 1.5 IQR, and the hollow circle is the mean. Forward and reverse scan *J*–*V* plots of different SAMs as the interlayer (e) without SnO_2 and (f) with SnO_2.

the champion FTO/SnO_2/C_{60}-PA device reached an η_{MPP} of 21.9% (see Note S4, Figure S16, and Table S11).

The worsened device FF and V_{oc} of the C_{60}-CA-modified devices could be due to the poor solvent wettability of the perovskite solution ontop of C_{60}-CA. Pinholes formed in the subsequently processed perovskite layer can result in reduced device shunt resistance and lower FF (Figure 2f). Due to their superior solar cell performance, we continue to investigate the SnO_2/C_{60}-PA devices, as compared to the neat SnO_2 devices in the remainder of the paper.

Although hysteresis per se is difficult to quantify since it is *J*–*V* scan-frequency-dependent,[26] performing *J*–*V* scans over a broad range of frequencies can reveal information about the ionic and electronic conductivity and the influence of ions within the solar cell device. Vallés-Pelarda et al.[27] have shown that there is a scan-frequency-dependent capacitive component

Table 1. Steady-State (ss) Statistical Parameters of n–i–p Devices Made with Different ETL Modifications[a]

Device ETL	ssV_{oc} (V)	ssJ_{sc} (mA/cm^2)	ssFF (%)	η_{MPP} (%)
FTO/SnO_2	1.04 ± 0.01	23.15 ± 0.38	76.8 ± 2.1	18.6 ± 0.7
FTO/SnO_2/C_{60}-CA	1.02 ± 0.01	23.51 ± 0.36	73.7 ± 5.2	17.8 ± 1.4
FTO/SnO_2/C_{60}-PA	1.06 ± 0.01	23.42 ± 0.27	78.6 ± 1.8	19.5 ± 0.5
FTO	0.61 ± 0.09	19.54 ± 8.62	55.9 ± 25.5	6.8 ± 4.5
FTO/C_{60}-CA	0.72 ± 0.07	23.32 ± 0.34	58.8 ± 6.7	9.9 ± 1.8
FTO/C_{60}-PA	0.80 ± 0.05	23.74 ± 0.14	71.4 ± 8.2	13.5 ± 2.2

[a]Average value ± standard deviation (8 devices per condition).

for n–i–p devices. To see if we can reveal any information about the difference between our control SnO_2 and C_{60}-PA-treated PSCs, we conduct "fast-hysteresis" measurements on the best devices, with scan frequencies ranging from 0.03 to 100 Hz. The applied voltage starts from forward bias near open-circuit (OC) and sweeps to short-circuit (SC) and then back toward and just past open-circuit again, as one cycle. The results of the parameters extracted from the *J*–*V* curves are presented in Figure 3.

The deviation of the J_{sc}, FF, and hence PCE values from Figure 2 is discussed in detail (see Note S5). We can see two features from the frequency-dependent *J*–*V* results. (1) Both the SnO_2 and the SnO_2/C_{60}-PA devices show a general trend of much lower performance parameters under the slowest frequency scans compared to the highest. (2) There is more hysteresis in the SnO_2 control device, where a "peak hysteresis" is observed in the 2–5 Hz medium frequency scan range. This is much less pronounced in the SnO_2/C_{60}-PA cells and occurs at a frequency close to 10 Hz. This peak hysteresis has been interpreted to correlate with the inverse of the average "drift-time" for ions across the perovskite absorber layer,[28,29] resulting in the maximum difference in ionic displacement between forward and reverse scanning directions. Hysteresis is likely caused by a combination of ion migration, interfacial recombination,[30,31] and the redistribution of ions under short-circuit conditions resulting in the inhibition of electronic charge extraction. Given that all other conditions in the two device stacks are identical, the results point to the improvement in the properties of the transport layer that reduces the impact of ionic movement.

While there is a consistent drop in TCSPC lifetime, PLQY, and SPV intensity for the device "half-stack" with C_{60}-PA modification, there is an increase in η_{MPP} and reduced hysteresis, indicating that the impact of ion diffusion and redistribution is likely to dominate the differences in device operation. While the slower surface photovoltage rise for the C_{60}-PA-modified samples may seem paradoxical with the reduced ionic losses we infer from the frequency-dependent *J*–*V* scans, this may originate from the nature of C_{60}. The phenomenon of fullerenes reducing hysteresis in PSCs is often observed.[27,32−34] Fullerenes are known to participate in halogen bonding,[35,36] and Ren et al.[37] have recently shown that fullerenes have the ability to capture I_3^- and I_2 that arise from I^- migration from the perovskite into the contacts. In the case of n–i–p devices where fullerene derivatives are processed on top of SnO_2, once I_3^- and I_2 have reached the C_{60}-SAMs, they may be captured at

https://doi.org/10.1021/acsenergylett.6c01485
ACS Energy Lett. 2026, 11, 6177−6186

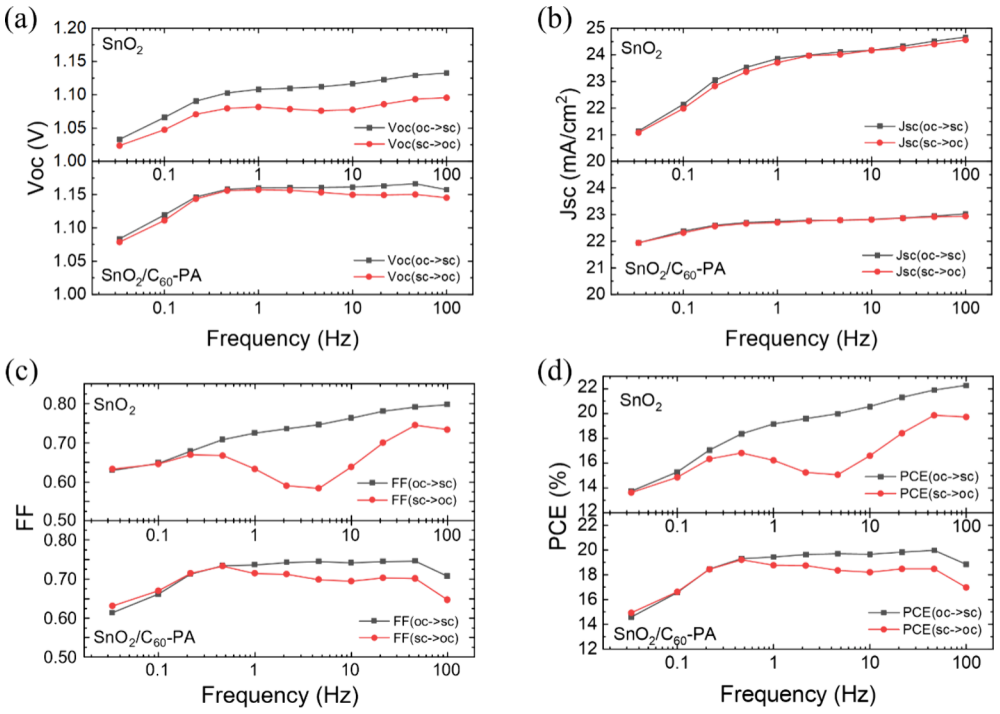

Figure 3. *J–V* parameters derived from scan-frequency-dependent "fast-hysteresis" measurements, showing (a) open-circuit voltage (V_{oc}), (b) short-circuit current density (J_{sc}), (c) fill factor (FF), and (d) power conversion efficiency (PCE).

the perovskite/C_{60}-SAM interface, inhibiting their migration back into the perovskite film when the electric field switches direction during the *J–V* scan routine, which may be responsible for the reduced negative impact from ion migration and device hysteresis. However, due to this mechanism, fullerenes may cause ion accumulation at the interface. Over time, fullerenes may accept electrons from I^- and reduce I^- to I_2 which could then represent a degradation loss product.

On the other hand, You et al.[24] suggested that when C_{60}-PA is mixed in the perovskite precursor solution and crystallized in the bulk, it can prevent halide segregation by passivating the grain boundaries through PA interacting with the perovskite cation/halide and fullerene interacting with the halide. Furthermore, You et al. also observed that moisture stability of the perovskite was improved, inferred to be due to the hydrophobic C_{60}-PA modification. Their modified perovskite was able to resist degradation to δ-$FAPbI_3$ and PbI_2 under high (70%) relative humidity.

To identify which effect may be dominating when we apply C_{60}-PA as an interfacial modification, we first study the effects of aging on the charge-carrier extraction and mobility at the ETL/$FAPbI_3$ interface. We performed optical-pump terahertz-probe (OPTP) photoconductivity to determine the sum of electron and hole mobilities[38−41] (Figure 4a,b). Samples were aged at 65 °C under full-spectrum AM 1.5G illumination (PMMA encapsulation only) for up to ∼350 h, with OPTP measurements acquired periodically throughout aging. We note that the effective short-range THz mobility Σϕμ (where ϕ is the photon-to-free-charge branching ratio) was determined immediately following a 400-nm pulsed photoexcitation. Given the steep Beer–Lambert profile upon the 400 nm excitation shown in Figure S17, Σϕμ is therefore mostly probing the perovskite near the ETL/perovskite interface, through which the pulse was incident. Figure 4a shows Σϕμ as a function of aging time. The initial Σϕμ values before aging (0 h) are similar for perovskite, SnO_2/perovskite, and SnO_2/C_{60}-PA/perovskite samples, on the order of 60–70 $cm^2\ V^{-1}\ s^{-1}$. With increasing aging time, the mobilities decrease for all samples, but for the SnO_2/C_{60}-PA/perovskite sample, a particularly accelerated decline is observed. Given that their bulk properties are similar, the observed decrease in the mobilities most likely arises from extrinsic factors such as an increase in charge-carrier scattering caused by a rise in the surface defect density at the perovskite/ETL interface. This result is consistent with the SPV results. While both the SnO_2/perovskite and SnO_2/C_{60}-PA/perovskite samples drop in SPV (Figure S15) after aging, the peak SPV intensity of C_{60}-PA-modified sample dropped more than the control sample without C_{60}-PA. In contrast to our expectations, we thus show that the presence of C_{60}-PA accelerates degradation of the material quality at the C_{60}-PA/$FAPbI_3$ interface, reducing the mobility experienced by charge carriers.

To understand how aging can affect the full devices, we fabricated n–i–p devices and aged them in the dark at 85 °C under a nitrogen atmosphere for over 2800 h and then encapsulated them and brought them into a light and elevated temperate aging box (Suntest CPS Plus), and aged at 70 ± 5 °C under AM 1.5G 76 mW/cm^2 irradiance for another 1080 h (Figure 4c,d). When the devices were brought into the light and 70 °C environmental chamber, the devices were aged under open-circuit conditions and brought outside periodically to test their performance under MPP for 30 s. We note that this is an especially harsh aging condition because the combination of light, heat, and V_{oc} creates the strongest driving force for ion migration, interfacial charge accumulation, and electrochemical instability.

https://doi.org/10.1021/acsenergylett.6c01485
ACS Energy Lett. 2026, 11, 6177−6186

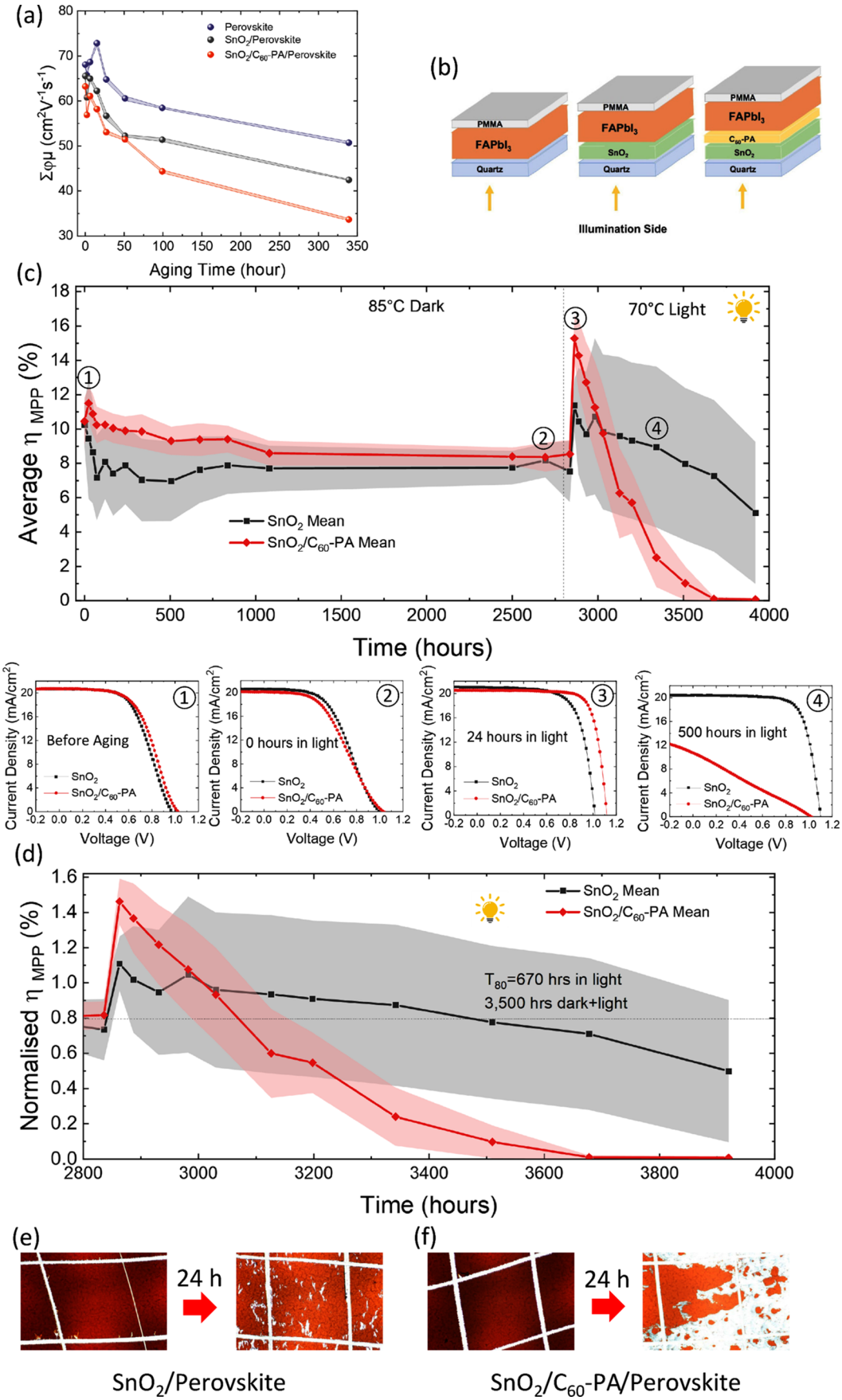

Figure 4. (a) Electron-hole sum mobility (Σϕμ) derived from OPTP spectroscopy of "half-stack" thin films aged in an aging box at 65 °C, AM 1.5G light over time. The shaded region represents the standard deviation band of 3 measurements. (b) Schematic of half-stack devices made with different

https://doi.org/10.1021/acsenergylett.6c01485
ACS Energy Lett. 2026, 11, 6177−6186

Figure 4. continued

ETL modifications. The thin films were illuminated from the quartz substrate side. (c) Average η_{MPP} of devices with different ETL modifications, first aged under an 85 °C dark, nitrogen environment for 2800 h and then taken into 70 ±5 °C AM 1.5G light for 1084 h. The device reverse scan *J*–*V* curves are shown at different stages of aging. (d) Normalized η_{MPP} (average of 8 devices) of devices normalized to the initial efficiency before any aging and zoomed into the last 1084 h under light and temperature (70 ± 5 °C, 0.76 suns). The shaded area in (c) and (d) represents their respective standard deviations. (e) and (f) photographs of ASTM peel-test samples, following the peel test before (left) and after (right) aging under 70 ± 5 °C AM 1.5G 76 mW cm^2 light for 24 h without encapsulation. (e) SnO_2/perovskite bilayer samples on FTO and (f) SnO_2/C_{60}-PA/perovskite bilayer samples on FTO.

Although the device stack used before had high η_{MPP}, doped Spiro-OMeTAD has been repeatedly observed to induce degradation in perovskite solar cells [42,43] and Au from neat Au electrodes can migrate into the device.[44] To ensure we are comparing the aging effects on the ETL/perovskite interface, rather than the other interfaces, the device stack was modified with more stable materials and passivation to test the long-term stability of the C_{60}-PA. The architecture used was FTO/ETL/$FA_{0.83}Cs_{0.17}Pb(I_{0.9}Br_{0.1})_3$/*n*-octylammonium-Br/PTAA/Cr/Au in which the ETL is either SnO_2/C_{60}-PA or SnO_2 with or without Al_2O_3 nanoparticles. Al_2O_3 was added to some devices to investigate whether it can aid wetting of the perovskite solution and improve the perovskite adhesion on the substrate (see Figure S18-S20).[45] 1-Butyl-1-methylpiperidinium tetrafluoroborate ($BMPBF_4$), an ionic stabilizing additive, is added into the perovskite to help stabilize it under temperature and light.[46]

With this more stable device structure, the initial power conversion efficiency was considerably lower, with an average just over 10%. In the dark at 85 °C, the SnO_2/C_{60}-PA devices appear to be more stable over the first thousand hours and even improve in efficiency initially. However, after around 2500 h, both types of cells have slowly degraded to between 8 and 9% efficiency. A closer inspection of the *J*–*V* curves evolution (Figures 4c and S21) reveals that under dark aging, the fill factor decreases over time and "s-kinks" emerge.

Surprisingly, following this thermal aging and upon exposure to light and temperature, the solar cells rapidly recover their FF losses, and the overall efficiency of both types of cells increased to values higher than their initial efficiency prior to any aging. Most significantly, the average efficiency of the SnO_2/C_{60}-PA devices increased to ∼15%. Surprisingly, the SnO_2 cells, without any Al_2O_3 were the most stable, exhibiting a T_{80}, aging time to 80% of the peak performance, of 477 h (T_{80} of initial performance is 670 h). This is a substantial lifetime for cells in the n–i–p configuration, which are usually much less stable than p–i–n cells.[47] In contrast, the SnO_2/C_{60}-PA devices degrade considerably faster, exhibit a T_{80} (80% of peak performance) lifetime of around 84 h from the point of light exposure (T_{80} of initial performance was 205 h), and have completely degraded in performance to ∼0% over the 1080 h aging under light and temperature. Al_2O_3 addition slightly improved the stability of SnO_2/C_{60}-PA devices but not enough to compete with SnO_2 only devices.

Upon visual inspection of the solar cells at the end of the entire 3900 h aging test (photographs in Figure S20), the SnO_2 devices (control devices) stayed much darker and appeared more "intact" as compared to any other type of device, including the SnO_2/C_{60}-PA and the SnO_2 with Al_2O_3 nanoparticles, which correlates with our performance degradation results. Aside from appearing lighter in color, the aged cells appeared hazy. This is likely to be due to partial delamination or voids forming at an interface between the ETL substrate and the perovskite absorber layer, where the lower refractive index "void-gaps" result in increased reflectivity and scattering.

As a first assessment of the "weakest interface" in these post-aged cells, we broke off the encapsulation glass from the SnO_2 and SnO_2/C_{60}-PA cells, to observe which layers were removed with the cover glass, and which remained adhered to the glass/FTO substrate. We show photographs of deconstructed cells in Figure S22. Quite convincingly, for the SnO_2 devices, the perovskite film remained predominantly adhered to the glass/FTO substrate, whereas for the SnO_2/C_{60}-PA devices, the perovskite layer was almost completely removed from the substrates in the regions below the metallic device electrodes. This is consistent with delamination occurring at the C_{60}-PA/perovskite interface and is the dominant cause for device degradation.

Finally, to quantify the impact of the ETL/perovskite interface upon adhesion following light and temperature aging, we aged "half stacks" constructed of Glass/FTO/ETL/Perovskite and performed an American Society for Testing and Materials (ASTM) standard peel test. We made crosshatch scratching patterns on these films and subsequently applied a standard ASTM tape on the film and then peeled the tape off at a near 180° angle. As shown in Figure 4e (left) and f (left), very little material is removed for both fresh films, which is encouraging for the starting adhesion strength of these layers. However, when we age these films in the 70 °C light aging box without encapsulation for 24 h and then apply the peel test, a significant amount of perovskite film is removed, especially for the SnO_2/C_{60}-PA-modified sample Figure 4f (right) compared to the film without C_{60}-PA Figure 4e (right). This direct peel test further confirms that the C_{60}-PA addition weakens the ETL/perovskite interface under the combined aging of light and heat. While the phosphoryl and hydroxyl groups of the C_{60}-PA binds strongly to SnO_2, the fullerene part of the C_{60}-PA only interacts weakly with the perovskite through halide–π or van der Waals interaction. The *J*–*V* curve evolution in Figure S21b is consistent with perovskite delaminating from the C_{60}-PA because, compared to the control device (Figure S21a), the C_{60}-PA device loses J_{sc} and FF over time while their V_{oc} values remain approximately constant throughout aging. This is consistent with a loss of contact area between the perovskite film and the ETL.

Hence, we have found that the C_{60}-PA SAM improves device efficiency by mitigating ion-induced device hysteresis and current loss, rather than enhancing charge transport. However, we have revealed that, under combined light and heat stress, the primary degradation of the C_{60}-PA-modified device is the (micro) delamination of the perovskite film from the ETL layer. This may result from iodide adsorption and accelerated I_2 generation at this interface as a consequence of the presence of C_{60}, since SnO_2 ETL-containing half-stacks and devices remain much more intact after aging.

https://doi.org/10.1021/acsenergylett.6c01485
ACS Energy Lett. 2026, 11, 6177−6186

Our findings also have implications for p–i–n perovskite solar cells, which usually employ fullerene derivatives as the ETLs. If we seek to employ organic electron-transport layers in perovskite solar cells, and especially SAMs,[48] then urgent work is required to increase the physical adhesion at these interfaces and inhibit weakening of these interfaces during aging. This may, for instance, be achieved through bifunctional SAMs that bind to both adjoining layers, with ETL-SAMs co-assembled with adhesion-promoting molecules,[49] or additional interfacial adhesion layers. However, if the mechanism is driven by the specific interaction of the organic electron-transport molecule with iodide, then this chemistry needs to be understood and mitigated through molecular selection or design.

■ ASSOCIATED CONTENT

Data Availability Statement

All relevant data are provided in the figures, tables, and Supplementary Information. Input files of the DFT calculations and optimized geometries are available on the Oxford University Research Archive.

Supporting Information

The Supporting Information is available free of charge at https://pubs.acs.org/doi/10.1021/acsenergylett.6c01485.

Experimental methods, including thin-film and solar cell fabrication, spectroscopic characterization and testing, further supporting discussion on chemical synthesis, DFT calculations, and GIWAXS, and additional references and figures (DOCX)

■ AUTHOR INFORMATION

Corresponding Author

Henry J. Snaith – *Department of Physics, University of Oxford, Clarendon Laboratory, Parks Road, Oxford OX1 3PU, U.K.*; orcid.org/0000-0001-8511-790X; Email: henry.snaith@physics.ox.ac.uk

Authors

Suer Zhou – *Department of Physics, University of Oxford, Clarendon Laboratory, Parks Road, Oxford OX1 3PU, U.K.*

Luca Gregori – *Computational Laboratory for Hybrid/Organic Photovoltaics (CLHYO), Istituto CNR di Scienze e Tecnologie Chimiche "Giulio Natta" (CNR-SCITEC), Via Elce di Sotto 8, Perugia 06123, Italy; Department of Chemistry, Biology and Biotechnology, University of Perugia, Perugia 06123, Italy*; orcid.org/0000-0002-0023-8313

Seongrok Seo – *Department of Physics, University of Oxford, Clarendon Laboratory, Parks Road, Oxford OX1 3PU, U.K.*; orcid.org/0009-0000-6032-2747

Raghunath R. Dasari – *School of Chemistry and Biochemistry and Center for Organic Photonics and Electronics, Georgia Institute of Technology, North Avenue, Atlanta, Georgia 30332, United States*; orcid.org/0000-0002-3237-7334

Jae Eun Lee – *Department of Physics, University of Oxford, Clarendon Laboratory, Parks Road, Oxford OX1 3PU, U.K.*

Edoardo Mosconi – *Computational Laboratory for Hybrid/Organic Photovoltaics (CLHYO), Istituto CNR di Scienze e Tecnologie Chimiche "Giulio Natta" (CNR-SCITEC), Via Elce di Sotto 8, Perugia 06123, Italy*

Heon Jin – *Department of Physics, University of Oxford, Clarendon Laboratory, Parks Road, Oxford OX1 3PU, U.K.*

Francesca Nunzi – *Computational Laboratory for Hybrid/Organic Photovoltaics (CLHYO), Istituto CNR di Scienze e Tecnologie Chimiche "Giulio Natta" (CNR-SCITEC), Via Elce di Sotto 8, Perugia 06123, Italy; Department of Chemistry, Biology and Biotechnology, University of Perugia, Perugia 06123, Italy*; orcid.org/0000-0003-0995-1497

Fengning Yang – *Department of Physics, University of Oxford, Clarendon Laboratory, Parks Road, Oxford OX1 3PU, U.K.*

Manuel Kober-Czerny – *Department of Physics, University of Oxford, Clarendon Laboratory, Parks Road, Oxford OX1 3PU, U.K.*; orcid.org/0000-0002-7807-3133

Alexandra J. Ramadan – *Department of Physics, University of Oxford, Clarendon Laboratory, Parks Road, Oxford OX1 3PU, U.K.; School of Mathematical and Physical Sciences, University of Sheffield, Hounsfield Road, Sheffield S3 7RH, U.K.*; orcid.org/0000-0003-4572-3459

Akash Dasgupta – *Department of Physics, University of Oxford, Clarendon Laboratory, Parks Road, Oxford OX1 3PU, U.K.*; orcid.org/0000-0002-7942-293X

Leonardo Pacifici – *Computational Laboratory for Hybrid/Organic Photovoltaics (CLHYO), Istituto CNR di Scienze e Tecnologie Chimiche "Giulio Natta" (CNR-SCITEC), Via Elce di Sotto 8, Perugia 06123, Italy*

Igal Levine – *Division Solar Energy, Helmholtz-Zentrum Berlin für Materialien und Energie GmbH, Hahn-Meitner-Platz 1, Berlin 14109, Germany; Institute of Chemistry and The Center for Nanoscience and Nanotechnology, The Hebrew University of Jerusalem, Jerusalem 9190401, Israel*; orcid.org/0000-0003-0406-2922

Joel Smith – *Department of Physics, University of Oxford, Clarendon Laboratory, Parks Road, Oxford OX1 3PU, U.K.*; orcid.org/0000-0001-6889-4408

Stephen Barlow – *School of Chemistry and Biochemistry and Center for Organic Photonics and Electronics, Georgia Institute of Technology, North Avenue, Atlanta, Georgia 30332, United States; Renewable and Sustainable Energy Institute, University of Colorado Boulder, 4001 Discovery Drive, Boulder, Colorado 80309, United States*; orcid.org/0000-0001-9059-9974

Laura M. Herz – *Department of Physics, University of Oxford, Clarendon Laboratory, Parks Road, Oxford OX1 3PU, U.K.*; orcid.org/0000-0001-9621-334X

Filippo De Angelis – *Computational Laboratory for Hybrid/Organic Photovoltaics (CLHYO), Istituto CNR di Scienze e Tecnologie Chimiche "Giulio Natta" (CNR-SCITEC), Via Elce di Sotto 8, Perugia 06123, Italy; Department of Chemistry, Biology and Biotechnology, University of Perugia, Perugia 06123, Italy; SKKU Institute of Energy Science and Technology (SIEST), Sungkyunkwan University, Suwon 440-746, South Korea*; orcid.org/0000-0003-3833-1975

Seth R. Marder – *School of Chemistry and Biochemistry and Center for Organic Photonics and Electronics, Georgia Institute of Technology, North Avenue, Atlanta, Georgia 30332, United States; Renewable and Sustainable Energy Institute, University of Colorado Boulder, 4001 Discovery Drive, Boulder, Colorado 80309, United States; Department of Chemical and Biological Engineering, University of Colorado Boulder, 3415 Colorado*

https://doi.org/10.1021/acsenergylett.6c01485
ACS Energy Lett. 2026, 11, 6177−6186

Avenue, Boulder, Colorado 80309, United States; Department of Chemistry, University of Colorado Boulder, 1606 Central Campus Mall, Boulder, Colorado 80309, United States

Complete contact information is available at: https://pubs.acs.org/doi/10.1021/acsenergylett.6c01485

Notes

The authors declare the following competing financial interest(s): H.J.S. is a co-founder and chief scientific advisor of Oxford PV Ltd.

■ ACKNOWLEDGMENTS

This work was part funded by EPSRC under the Application Targeted and Integrated Photovoltaics (ATIP SWANSEA project grant #EP/T028513/1) and part funded by the Office of Naval Research (Award #N00014-20-1-2587) and the Office of Naval Research-Global (subaward #UWSC12114). The synthesis of the C_{60}-PA at Georgia Tech, as well as the contributions of S.B. and S.R.M. to editing the manuscript, was supported by the Office of Naval Research through N00014-20-1-2587 and N00014-24-1-2115, respectively. This work acknowledges funding from the Presidency of the Council of Ministers (Presidenza del Consiglio dei Ministri)—Department for Cohesion Policies and the South (Dipartimento per le politiche di coesione e per il sud), under the UMbriaTECH—Umbria Materials TECHnology district project (CUP E67G23000220001), and acknowledges funding from the Italian Ministry of Environment and Energy Security in the framework of the Project GoPV (CSEAA_00011) for Research on the Electric System. S.Z. thanks the EU-H2020 PeroCUBE under grant agreement #861985 for postdoctoral funding support for the writing of the paper. A.R.acknowledges the funding from EPSRC EP/X039285/1 for support of the XPS and UPS measurements and analysis of this work. I.L. thanks the AiF project (ZIM-KK5085302DF0) for financial support.

■ REFERENCES

(1) *Best Research-Cell Efficiency Chart | Photovoltaic Research | NREL*. https://www.nrel.gov/pv/cell-efficiency.html (accessed May 2026).

(2) Yoo, J. J.; Seo, G.; Chua, M. R.; Park, T. G.; Lu, Y.; Rotermund, F.; Kim, Y.-K.; Moon, C. S.; Jeon, N. J.; Correa-Baena, J.-P.; Bulović, V.; Shin, S. S.; Bawendi, M. G.; Seo, J. Efficient Perovskite Solar Cells via Improved Carrier Management. *Nature* **2021**, *590* (7847), 587–593.

(3) Li, Z.; Wang, C.; Sun, P. P.; Zhang, Z.; Zhou, Q.; Du, Y.; Xu, J.; Chen, Y.; Xiong, Q.; Ding, L.; Nazeeruddin, M. K.; Gao, P. In-Situ Peptization of WO_3 in Alkaline SnO_2 Colloid for Stable Perovskite Solar Cells with Record Fill-Factor Approaching the Shockley–Queisser Limit. *Nano Energy* **2022**, *100*, 107468.

(4) Jung, E. H.; Chen, B.; Bertens, K.; Vafaie, M.; Teale, S.; Proppe, A.; Hou, Y.; Zhu, T.; Zheng, C.; Sargent, E. H. Bifunctional Surface Engineering on SnO_2 Reduces Energy Loss in Perovskite Solar Cells. *ACS Energy Lett.* **2020**, *5* (9), 2796–2801.

(5) Godinho, K. G.; Walsh, A.; Watson, G. W. Energetic and Electronic Structure Analysis of Intrinsic Defects in SnO_2. *J. Phys. Chem. C* **2009**, *113* (1), 439–448.

(6) Tumen-Ulzii, G.; Matsushima, T.; Klotz, D.; Leyden, M. R.; Wang, P.; Qin, C.; Lee, J. W.; Lee, S. J.; Yang, Y.; Adachi, C. Hysteresis-Less and Stable Perovskite Solar Cells with a Self-Assembled Monolayer. *Commun. Mater.* **2020**, *1* (1), 1–7.

(7) Liu, K.; Tian, C.; Liang, Y.; Luo, Y.; Xie, L.; Wei, Z. Progress toward Understanding the Fullerene-Related Chemical Interactions in Perovskite Solar Cells. *Nano Res.* **2022**, *15* (8), 7139–7153.

(8) Liu, K.; Chen, S.; Wu, J.; Zhang, H.; Qin, M.; Lu, X.; Tu, Y.; Meng, Q.; Zhan, X. Fullerene Derivative Anchored SnO_2 for High-Performance Perovskite Solar Cells. *Energy Environ. Sci.* **2018**, *11* (12), 3463–3471.

(9) Wang, J.; Datta, K.; Weijtens, C. H. L.; Wienk, M. M.; Janssen, R. A. J. Insights into Fullerene Passivation of SnO_2 Electron Transport Layers in Perovskite Solar Cells. *Adv. Funct. Mater.* **2019**, *29* (46), 1905883.

(10) Ke, W.; Zhao, D.; Xiao, C.; Wang, C.; Cimaroli, A. J.; Grice, C. R.; Yang, M.; Li, Z.; Jiang, C.-S.; Al-Jassim, M.; Zhu, K.; Kanatzidis, M. G.; Fang, G.; Yan, Y. Cooperative Tin Oxide Fullerene Electron Selective Layers for High-Performance Planar Perovskite Solar Cells. *J. Mater. Chem. A* **2016**, *4* (37), 14276–14283.

(11) Cao, T.; Chen, K.; Chen, Q.; Zhou, Y.; Chen, N.; Li, Y. Fullerene Derivative-Modified SnO_2 Electron Transport Layer for Highly Efficient Perovskite Solar Cells with Efficiency over 21%. *ACS Appl. Mater. Interfaces.* **2019**, *11* (37), 33825–33834.

(12) Wojciechowski, K.; Leijtens, T.; Siprova, S.; Schlueter, C.; Hörantner, M. T.; Wang, J. T.-W.; Li, C.-Z.; Jen, A. K.-Y.; Lee, T.-L.; Snaith, H. J. C_{60} as an Efficient N-Type Compact Layer in Perovskite Solar Cells. *J. Phys. Chem. Lett.* **2015**, *6* (12), 2399–2405.

(13) Xue, D.; Wakahara, T.; Marumoto, K.; Tsukagoshi, K. High Charge Transfer from C_{60} Pyrrolidine Tris-Acid to SnO_2 Electron Transport Layer Directly Observed by ESR Spectroscopy. *ACS Appl. Energy Mater.* **2023**, *6* (4), 2434–2439.

(14) Huang, S. K.; Wang, Y. C.; Ke, W. C.; Kao, Y. T.; She, N. Z.; Li, J. X.; Luo, C. W.; Yabushita, A.; Wang, D. Y.; Chang, Y. J.; Tsukagoshi, K.; Chen, C. W. Unravelling the Origin of the Photocarrier Dynamics of Fullerene-Derivative Passivation of SnO_2 Electron Transporters in Perovskite Solar Cells. *J. Mater. Chem. A* **2020**, *8* (44), 23607–23616.

(15) Liu, S.; Li, J.; Xiao, W.; Chen, R.; Sun, Z.; Zhang, Y.; Lei, X.; Hu, S.; Kober-Czerny, M.; Wang, J.; Ren, F.; Zhou, Q.; Raza, H.; Gao, Y.; Ji, Y.; Li, S.; Li, H.; Qiu, L.; Huang, W.; Zhao, Y.; Xu, B.; Liu, Z.; Snaith, H. J.; Park, N.-G.; Chen, W. Buried Interface Molecular Hybrid for Inverted Perovskite Solar Cells. *Nature* **2024**, *632* (8025), 536–542.

(16) Zhao, K.; Liu, Q.; Yao, L.; Değer, C.; Shen, J.; Zhang, X.; Shi, P.; Tian, Y.; Luo, Y.; Xu, J.; Zhou, J.; Jin, D.; Wang, S.; Fan, W.; Zhang, S.; Chu, S.; Wang, X.; Tian, L.; Liu, R.; Zhang, L.; Yavuz, I.; Wang, H.; Yang, D.; Wang, R.; Xue, J. Peri-Fused Polyaromatic Molecular Contacts for Perovskite Solar Cells. *Nature* **2024**, *632* (8024), 301–306.

(17) Zheng, Y.; Li, Y.; Zhuang, R.; Wu, X.; Tian, C.; Sun, A.; Chen, C.; Guo, Y.; Hua, Y.; Meng, K.; Wu, K.; Chen, C.-C. Towards 26% Efficiency in Inverted Perovskite Solar Cells via Interfacial Flipped Band Bending and Suppressed Deep-Level Traps. *Energy Environ. Sci.* **2024**, *17* (3), 1153–1162.

(18) Jiang, W.; Wang, D.; Shang, W.; Li, Y.; Zeng, J.; Zhu, P.; Zhang, B.; Mei, L.; Chen, X.-K.; Xu, Z.-X.; Lin, F. R.; Xu, B.; Jen, A. K.-Y. Spin-Coated and Vacuum-Processed Hole-Extracting Self-Assembled Multilayers with H-Aggregation for High-Performance Inverted Perovskite Solar Cells. *Angew. Chem. Int. Ed. Engl.* **2024**, *64* (45), e202411730.

(19) Zheng, D.; Miao, T.; Zhang, Z.; Vegso, K.; Zhu, T.; Wang, L.; Xu, Z.; Ullah, S.; Slusna, L. P.; Kim, G.; Hu, D.; Fong, P.; Liu, Z.; Lv, J.; Siffalovic, P.; Mrkyvkova, N.; Chen, W.; Abate, A.; Li, M.; Li, G. Omnidirectional Ionic Locking Network for Stable Perovskite Photovoltaics. *Nat. Photonics* **2026**, .

(20) Xiong, Z.; Zhang, Q.; Cai, K.; Zhou, H.; Song, Q.; Han, Z.; Kang, S.; Li, Y.; Jiang, Q.; Zhang, X.; You, J. Homogenized Chlorine Distribution for >27% Power Conversion Efficiency in Perovskite Solar Cells. *Science* **2025**, *390* (6773), 638–642.

(21) Jiang, E.; Ai, Y.; Yan, J.; Li, N.; Lin, L.; Wang, Z.; Shou, C.; Yan, B.; Zeng, Y.; Sheng, J.; Ye, J. Phosphate-Passivated SnO_2 Electron Transport Layer for High-Performance Perovskite Solar Cells. *ACS Appl. Mater. Interfaces* **2019**, *11* (40), 36727–36734.

(22) Wagstaffe, M.; Thomas, A. G.; Jackman, M. J.; Torres-Molina, M.; Syres, K. L.; Handrup, K. An Experimental Investigation of the Adsorption of a Phosphonic Acid on the Anatase TiO_2(101) Surface. *J. Phys. Chem. C* **2016**, *120* (3), 1693–1700.
(23) Hau, S. K.; Cheng, Y.-J.; Yip, H.-L.; Zhang, Y.; Ma, H.; Jen, A. K.-Y. Effect of Chemical Modification of Fullerene-Based Self-Assembled Monolayers on the Performance of Inverted Polymer Solar Cells. *ACS Appl. Mater. Interfaces* **2010**, *2* (7), 1892–1902.
(24) You, S.; Zeng, H.; Liu, Y.; Han, B.; Li, M.; Li, L.; Zheng, X.; Guo, R.; Luo, L.; Li, Z.; Zhang, C.; Liu, R.; Zhao, Y.; Zhang, S.; Peng, Q.; Wang, T.; Chen, Q.; Eickemeyer, F. T.; Carlsen, B.; Zakeeruddin, S. M.; Mai, L.; Rong, Y.; Grätzel, M.; Li, X. Radical Polymeric P-Doping and Grain Modulation for Stable, Efficient Perovskite Solar Modules. *Science* **2023**, *379* (6629), 288–294.
(25) Gregori, L.; Meggiolaro, D.; De Angelis, F. Quantifying the Effect of Interfacial Dipoles on the Energy Level Alignment of Metal-Halide Perovskites. *ACS Energy Lett.* **2024**, *9* (11), 5329–5333.
(26) Habisreutinger, S. N.; Noel, N. K.; Snaith, H. J. Hysteresis Index: A Figure without Merit for Quantifying Hysteresis in Perovskite Solar Cells. *ACS Energy Lett.* **2018**, *3* (10), 2472–2476.
(27) Valles-Pelarda, M.; Hames, B. C.; García-Benito, I.; Almora, O.; Molina-Ontoria, A.; Sánchez, R. S.; Garcia-Belmonte, G.; Martín, N.; Mora-Sero, I. Analysis of the Hysteresis Behavior of Perovskite Solar Cells with Interfacial Fullerene Self-Assembled Monolayers. *J. Phys. Chem. Lett.* **2016**, *7* (22), 4622–4628.
(28) Richardson, G.; O'Kane, S. E. J.; Niemann, R. G.; Peltola, T. A.; Foster, J. M.; Cameron, P. J.; Walker, A. B. Can Slow-Moving Ions Explain Hysteresis in the Current–Voltage Curves of Perovskite Solar Cells? *Energy Environ. Sci.* **2016**, *9* (4), 1476–1485.
(29) Jacobs, D. A.; Shen, H.; Pfeffer, F.; Peng, J.; White, T. P.; Beck, F. J.; Catchpole, K. R. The Two Faces of Capacitance: New Interpretations for Electrical Impedance Measurements of Perovskite Solar Cells and Their Relation to Hysteresis. *J. Appl. Phys.* **2018**, *124* (22), 225702.
(30) van Reenen, S.; Kemerink, M.; Snaith, H. J. Modeling Anomalous Hysteresis in Perovskite Solar Cells. *J. Phys. Chem. Lett.* **2015**, *6* (19), 3808–3814.
(31) Calado, P.; Telford, A. M.; Bryant, D.; Li, X.; Nelson, J.; O'Regan, B. C.; Barnes, P. R. F. Evidence for Ion Migration in Hybrid Perovskite Solar Cells with Minimal Hysteresis. *Nat. Commun.* **2016**, *7* (1), 13831.
(32) Shao, Y.; Xiao, Z.; Bi, C.; Yuan, Y.; Huang, J. Origin and Elimination of Photocurrent Hysteresis by Fullerene Passivation in $CH_3NH_3PbI_3$ Planar Heterojunction Solar Cells. *Nat. Commun.* **2014**, *5* (1), 5784.
(33) Xu, J.; Buin, A.; Ip, A. H.; Li, W.; Voznyy, O.; Comin, R.; Yuan, M.; Jeon, S.; Ning, Z.; McDowell, J. J.; Kanjanaboos, P.; Sun, J.-P.; Lan, X.; Quan, L. N.; Kim, D. H.; Hill, I. G.; Maksymovych, P.; Sargent, E. H. Perovskite–Fullerene Hybrid Materials Suppress Hysteresis in Planar Diodes. *Nat. Commun.* **2015**, *6* (1), 7081.
(34) Fang, Y.; Bi, C.; Wang, D.; Huang, J. The Functions of Fullerenes in Hybrid Perovskite Solar Cells. *ACS Energy Lett.* **2017**, *2* (4), 782–794.
(35) King, R. B. *Encyclopedia of Inorganic Chemistry*, nd edition; Wiley, **2005**.
(36) Hirsch, A.; Brettreich, M. *Fullerenes: Chemistry and Reactions*; Wiley, **2006**; pp 267-284.
(37) Ren, X.; Wang, J.; Lin, Y.; Wang, Y.; Xie, H.; Huang, H.; Yang, B.; Yan, Y.; Gao, Y.; He, J.; Huang, J.; Yuan, Y. Mobile Iodides Capture for Highly Photolysis- and Reverse-Bias-Stable Perovskite Solar Cells. *Nat. Mater.* **2024**, *23* (6), 810–817.
(38) Motti, S. G.; Kober-Czerny, M.; Righetto, M.; Holzhey, P.; Smith, J.; Kraus, H.; Snaith, H. J.; Johnston, M. B.; Herz, L. M. Exciton Formation Dynamics and Band-Like Free Charge-Carrier Transport in 2D Metal Halide Perovskite Semiconductors. *Adv. Funct. Mater.* **2023**, *33* (32), No. 2300363.
(39) Johnston, M. B.; Herz, L. M. Hybrid Perovskites for Photovoltaics: Charge-Carrier Recombination, Diffusion, and Radiative Efficiencies. *Acc. Chem. Res.* **2016**, *49* (1), 146–154.
(40) Ulatowski, A. M.; Herz, L. M.; Johnston, M. B. Terahertz Conductivity Analysis for Highly Doped Thin-Film Semiconductors. *J. Infrared Millimeter Terahertz Waves* **2020**, *41* (12), 1431–1449.
(41) Buizza, L. R. V.; Sansom, H. C.; Wright, A. D.; Ulatowski, A. M.; Johnston, M. B.; Snaith, H. J.; Herz, L. M. Interplay of Structure, Charge-Carrier Localization and Dynamics in Copper-Silver-Bismuth-Halide Semiconductors. *Adv. Funct. Mater.* **2022**, *32* (6), 2108392.
(42) Luo, Q.; Zhang, Y.; Liu, C.; Li, J.; Wang, N.; Lin, H. Iodide-Reduced Graphene Oxide with Dopant-Free Spiro-OMeTAD for Ambient Stable and High-Efficiency Perovskite Solar Cells. *J. Mater. Chem. A* **2015**, *3* (31), 15996–16004.
(43) Sanchez, R. S.; Mas-Marza, E. Light-Induced Effects on Spiro-OMeTAD Films and Hybrid Lead Halide Perovskite Solar Cells. *Sol. Energy Mater. Sol. Cells* **2016**, *158*, 189–194.
(44) Domanski, K.; Correa-Baena, J. P.; Mine, N.; Nazeeruddin, M. K.; Abate, A.; Saliba, M.; Tress, W.; Hagfeldt, A.; Grätzel, M. Not All That Glitters Is Gold: Metal-Migration-Induced Degradation in Perovskite Solar Cells. *ACS Nano* **2016**, *10* (6), 6306–6314.
(45) Schultes, M.; Giesbrecht, N.; Küffner, J.; Ahlswede, E.; Docampo, P.; Bein, T.; Powalla, M. Universal Nanoparticle Wetting Agent for Upscaling Perovskite Solar Cells. *ACS Appl. Mater. Interfaces* **2019**, *11* (13), 12948–12957.
(46) Lin, Y. H.; Sakai, N.; Da, P.; Wu, J.; Sansom, H. C.; Ramadan, A. J.; Mahesh, S.; Liu, J.; Oliver, R. D. J.; Lim, J.; Aspitarte, L.; Sharma, K.; Madhu, P. K.; Morales-Vilches, A. B.; Nayak, P. K.; Bai, S.; Gao, F.; Grovenor, C. R. M.; Johnston, M. B.; Labram, J. G.; Durrant, J. R.; Ball, J. M.; Wenger, B.; Stannowski, B.; Snaith, H. J. A Piperidinium Salt Stabilizes Efficient Metal-Halide Perovskite Solar Cells. *Science* **2020**, *369* (6499), 96–102.
(47) McMeekin, D. P.; Holzhey, P.; Fürer, S. O.; Harvey, S. P.; Schelhas, L. T.; Ball, J. M.; Mahesh, S.; Seo, S.; Hawkins, N.; Lu, J.; Johnston, M. B.; Berry, J. J.; Bach, U.; Snaith, H. J. Intermediate-Phase Engineering via Dimethylammonium Cation Additive for Stable Perovskite Solar Cells. *Nat. Mater.* **2023**, *22* (1), 73–83.
(48) Dai, Z.; Yadavalli, S. K.; Chen, M.; Abbaspourtamijani, A.; Qi, Y.; Padture, N. P. Interfacial Toughening with Self-Assembled Monolayers Enhances Perovskite Solar Cell Reliability. *Science* **2021**, *372* (6542), 618–622.
(49) Dai, Z.; You, S.; Chakraborty, D.; Li, S.; Zhang, Y.; Ranka, A.; Barlow, S.; Berry, J. J.; Marder, S. R.; Guo, P.; Qi, Y.; Zhu, K.; Padture, N. P. Connecting Interfacial Mechanical Adhesion, Efficiency, and Operational Stability in High Performance Inverted Perovskite Solar Cells. *ACS Energy Lett.* **2024**, *9* (4), 1880–1887.

https://doi.org/10.1021/acsenergylett.6c01485
ACS Energy Lett. 2026, 11, 6177–6186